

# Modeling and hexahedral meshing of arterial networks from centerlines

Méghane Decroocq<sup>1,2,4,5,6</sup>, Carole Frindel<sup>1,5</sup>, Makoto Ohta<sup>4,5</sup>, Guillaume Lavoué<sup>2,3</sup>

<sup>1</sup> CREATIS, Université Lyon1, CNRS UMR5220, INSERM U1206, INSA-Lyon, 69621 Villeurbanne, France

<sup>2</sup> LIRIS, CNRS UMR 5205, F-69621, France

<sup>3</sup> Ecole Centrale de Lyon, France

<sup>4</sup> ELyTMaX IRL3757, CNRS, INSA Lyon, Centrale Lyon, Université Claude Bernard Lyon 1, Tohoku University, 980-8577, Sendai, Japan

<sup>5</sup> Institute of Fluid Science, Tohoku University, 2-1-1, Katahira, Aoba-ku, Sendai, Miyagi 980-8577, Japan

<sup>6</sup> Graduate School of Biomedical Engineering, Tohoku University, 6-6 Aramaki-aza-aoba, Aoba-ku, Sendai, Miyagi 980-8579, Japan

Corresponding Author: *carole.frindel@creatis.insa-lyon.fr*

## Abstract

Computational fluid dynamics (CFD) simulation provides valuable information on blood flow from the vascular geometry. However, it requires to extract accurate models of arteries from low resolution medical images, which remains challenging. Centerline-based representation is widely used to model large vascular networks with small vessels, as it enables manual editing and encodes the topological information. In this work, we propose an automatic method to generate an hexahedral mesh suitable for CFD directly from centerlines. The proposed method is an improvement of the state-of-the-art in terms of robustness, mesh quality and reproducibility.

Both the modeling and meshing tasks are addressed. A new vessel model based on penalized splines is proposed to overcome the limitations inherent to the centerline representation, such as noise and sparsity. Bifurcations are reconstructed using a physiologically accurate parametric model that we extended to planar n-furcations. Finally, a volume mesh with structured, hexahedral and flow oriented cells is produced from the proposed vascular network model.

The proposed method offers a better robustness and mesh quality than the state-of-the-art methods. As it combines both modeling and meshing techniques, it can be applied to edit the geometry and topology of vascular models effortlessly to study the impact on hemodynamics. We demonstrate the efficiency of our method by entirely meshing a dataset of 60 cerebral vascular networks. 92% of the vessels and 83% of the bifurcations where mesh without defects needing manual intervention, despite the challenging aspect of the input data. The source code will be released publicly.

**Keywords:** Arterial network, Centerlines, Hexahedral mesh, Computational fluid dynamics

## Introduction

Vascular diseases, such as stroke, can cause severe disability or death [30]. The relationship between the topology and geometry of the vascular network and the onset and the outcome of the pathology is increasingly investigated in the literature. Computational fluid dynamics is a key tool for this type of study, as it provides information on the hemodynamics from the vessel geometry [33, 36]. Numerical simulation requires a smooth, anatomically accurate model of the arterial wall to give reliable results. In the finite element method, the shape of the cells inside the volume also affects the simulations. Due to their ability to mesh automatically very complex shapes, tetrahedral cells are widely used. However, unstructured tetrahedral cells lead to higher computational cost and less accurate results than flow-oriented, structured hexahedral cells, as demonstrated by [39], [10] and [13]. Two main approaches used to address the meshing of vascular networks are segmentation-based and centerline-based methods.

The segmentation of magnetic resonance angiography (MRA) im-

ages is a non-invasive way to access patient-specific vasculature. A lot of effort was put in order to develop efficient vessel enhancing filters and to improve the segmentation methods [22, 27]. However, it remains a challenging task when it comes to large networks with voxel-sized vessels [25]. Besides, a good segmentation does not guarantee the accuracy of the network topology (e.g vessels merging due to the image resolution, disconnected vessels), and geometry (e.g bumps caused by voxelization). The segmentation result is generally meshed with tetrahedral elements and hexahedral remeshing is not straightforward.

Following the tubularity assumption, vessels can be reduced to a centerline-radius description. Segmentation-based and centerline-based models complement each others, centerline extraction being used as a pre-processing or post-processing of segmentation. Many methods to extract vessel skeletons from binary or raw images were proposed in the literature [34, 17]. As opposed to image segmentation, centerline-based representation advantageously incorporates the network topology and enables manual extraction and editing. This simplified representation is more suitable to the construction of

big databases of large vascular networks [40] or the creation of ideal models. As it encodes the vessel orientation, it has a high potential for the creation of meshes with flow-oriented, hexahedral cells. Nevertheless, the representation of vessels by centerlines lowers the geometrical information content ; depending on the extraction method, only a limited number of data points are used and noise can be introduced in the dataset. It causes inaccuracy in the shape of the vessels and in the position and geometry of bifurcations. These limitations make it difficult to reconstruct a smooth and physiologically accurate surface model that matches the requirements of numerical simulation.

In this work, we propose a method overcoming the limitations of centerlines to generate a high quality mesh ready for CFD. The input data is presented in section 3. Section 2 reviews the state-of-the-art methods in hexahedral meshing of vessels and surface reconstruction from centerlines. In section 4, we introduce a mathematical model to represent vessels as tubes, based on the approximation of centerline data by penalized splines. The proposed approximation framework allows for the combination of the spatial coordinates and radius in a single function. It is shown to be robust to noise and low sampling of data point, compared to other conventional approximation methods [28, 11]. The vessel model is combined with a physiological parametric model of bifurcation proposed by Zakaria et al. [42] to form a what we call a parametric arterial network. In the section 5, we present a method to create a structured hexahedral surface and volume mesh with flow oriented cells from the arterial network model detailed in the previous section. Original relaxation and smoothing steps are introduced to improve the quality of the cells without deforming the model shape. The meshing is fast and fully automatic, which opens the way to numerical simulation in large networks. As the modeling and meshing steps are intertwined, the proposed framework enables to easily and inexpensively edit the topology of the networks to study its influence on blood flow. In section 7, we use our method to mesh a database of 60 large cerebral networks. Other applications such as pathology modeling and hexahedral remeshing are also presented.

## 2 Related work

### 2.1 Hexahedral meshing

Hexahedral meshing has been investigated over the past years as it offers many advantages. It better capture the underlying topology of the object with a lower cell-density, and bridges the gap between representation and physical simulation, as it simplifies the boundary layer creation and domain discretization, and provides a basis for NURBS modeling [43]. Hexahedral meshing is however limited by a far more complex generation process than standard tetrahedral meshes. In the application to arterial network, the main challenge is the treatment of bifurcations. In the literature, this task was addressed by a two-step pipeline ; the bifurcations are first decomposed into three branches, then the hexahedral mesh is generated using the decomposition.

A variety of method were proposed to obtain a robust branch decomposition. De Santis et al. introduced semi-automatic methods, ranging from manual selection of the most relevant slices of the input surface mesh [10], user defined bifurcation coordinate system

[8], to the generation and adjustment of a block-structure representation of the network [9]. Automatic methods are based on Voronoi diagram [4], resolution of the Laplace's equation [37], random-walk algorithm [41] or branching templates [43] or parametric models [13]. The hexahedral meshing can then be created from the decomposition through various techniques ; Copper scheme in the work of [4], template grid sweeping for [37], [43] and [13], Bezier spline modeling followed by an iso-parametric transformation of a template mesh [8], projection and refinement of block-structures [9], Laplacian-based harmonic functions combined with Catmull-Clark subdivision [41].

There are limitations to the application of the described methods to our purpose. First, they often rely on manual intervention, which is limiting when applied to large datasets of complex vascular networks. The automatic methods proposed involve complex algorithms, and only [8] provided their code through the user-friendly interface PyFormex, which enables to generate hexahedral meshes semi-automatically from a single bifurcation vascular geometry. Moreover, only [13] use centerlines as input, and they are low noise centerlines extracted from a surface mesh using VMTK. The other methods require a tetrahedral surface mesh as input for the branch decomposition and the meshing steps. They can not be applied directly from realistic centerlines (both sparse and noisy), as those tackled by this work. The application of such hexahedral meshing methods to centerlines would require a continuous and accurate reconstruction of the vascular surface to be produced first.

### 2.2 Vascular modeling and reconstruction from centerlines

In this section, we review the methods used to recreate an accurate vascular surface from centerline information. The main issues to overcome in this task arise from the defects commonly observed in the vascular centerline extracted from medical images ; local discontinuities causing a lack of information - especially at the bifurcation parts -, noise due to the voxelization. In this context, the smoothness of the vessel surface and the accurate reconstruction of the bifurcation part are important locks. The reconstruction methods can be divided in explicit methods, where a tetrahedral mesh of the surface is produced, and implicit methods where the surface is represented by implicit functions. Implicit methods employs radial basis functions [18], implicit extrusion surfaces [19] or local implicit modeling [23] to reconstruct vascular networks from medical images. If they stand out by their ability to reconstruct complex branching topology, they are less suited for hexahedral meshing than explicit methods.

In explicit methods, the vessel surface is obtained by sweeping along the centerline. The quality of the reconstruction depends on the way centerline points are approximated, usually with Bezier or spline functions. Details of the approximation methods, in particular the accuracy of the tangent estimation and the robustness to noise were not given in previous studies. Various bifurcation models were proposed. In the work of [24] and [12], the three branches of the bifurcation are modeled separately and joined at the bifurcation center. The junction is then blended to restore the continuity, by a subdivision scheme for [24] and Bezier segments for [12]. This geometric model is particularly suited for hexahedral meshing, as the junction can be used as branch decomposition. However, it depends on the

accuracy of the position of the bifurcation center and the tangent of the branches, which is hard to estimate correctly from centerlines.

Besides, [16] and [14] modeled bifurcations using three tubes connecting the inlet and outlet sections. A half of each section of the tube is meshed by sweeping and the hole left in the middle is filled afterwards. Their method guarantees the smoothness of the model, but results in unnatural looking bifurcations. Finally, [42] proposed a physiologic model where the bifurcations are represented by two merged tubes. It was validated with regards to both the accuracy of the anatomy and of the CFD simulations. It does not rely on the geometrical center of the bifurcation, but on a set of physiological parameters (apex, apical sections, inlet and outlet sections). The hexahedral meshing is less straightforward from this model than the geometric model presented in the previous paragraph but it shows more anatomical realism. In [42], the authors extracted the model parameters from a surface mesh, they did not suggest a way to extract them from centerlines.

In this work, our purpose is to meet the challenges arising from this state-of-the-art with a framework integrating modeling and hexahedral meshing. Our method does not require to generate a tetrahedral mesh at any stage of its application. It produces an hexahedral mesh from centerlines only, with a controlled trade-off between smoothness and proximity to the input centerline data points, and a realistic bifurcation shape with customizable physiological parameters as proposed by [42].

### 3 Input data

The input vessel centerlines we consider are composed of set of data points with three spatial coordinates (x,y,z), radius value (r), and the connectivity between points. Data points might have several successors (e.g bifurcations). A point with  $n$  successors is a  $n$ -furcation. The centerlines are stored using the swc format or VMTK format of [21]. In this work, we use centerlines from two publicly available datasets. The Aneurisk database [3] provides 3D models of the main arteries of the circle of Willis for patients with aneurism. High resolution centerlines were extracted from the surface meshes using VMTK software. The BraVa database [40] gathers the centerlines of the whole cerebral network for 60 patients. To create this dataset, the data points were manually placed by medical doctors on medical images using imageJ plugin Neurite Tracer [26] and the radius was automatically computed. As a result, the data points have a lower spatial resolution and are prone to errors and noise.

## 4 Modeling

### 4.1 Vessels

In this part, we focus on the modeling of vessels from centerline data; the case of bifurcations is addressed in the next section. Different models of centerlines were proposed in the literature, based on the approximation of data points by Bezier segments [13], regression splines [24], free knot regression splines or local polynomial smoothing [32]. Only [32] gives the detail of the implementation of the approximation method and provides a thorough study

of the accuracy of their model in regard with the spatial coordinates and the derivatives. Actually, the accuracy of both the first and second derivatives is crucial because the vessel curvature impacts the haemodynamics [31]. Moreover, meshing techniques are often based on the normals of the centerline [24, 13]. It is important to note that the proposed approximation methods [32, 24, 13] focus on the spatial coordinates of the centerlines, excluding the radius. In this work, we propose a parametric model of vessels based on approximation by penalized splines. Our approximation method enables to combine the spatial coordinates and radius in a single function with physiologically accurate values and derivatives and is robust to noise and low sampling of the input data.

#### 4.1.1 Penalized splines

We want to approximate a set of  $m$  points  $\{D_0, D_1, \dots, D_{m-1}\}$  with 4 coordinates  $(x, y, z, r)$ , using a spline function  $s$  defined as

$$s(u) = \sum_{i=0}^{n-1} N_{i,p}(u)P_i, \quad (1)$$

for  $u \in [0, 1]$ , where  $N_{i,p}$  is the  $i$ th basis spline function of order  $p$  and  $\{P_0, P_1, \dots, P_{n-1}\}$  the  $n$  control points of the spline. The shape of the basis splines functions and therefore the part of the spline controlled by a given control point is given by a set of knots.

The main challenge in the approximation of noisy data is to find the optimal balance between the proximity of the curve to data points and the smoothness of the curve (i.e. the accuracy of the derivatives). There are two main approaches to control the smoothness of a spline function. The first is to change the number of control points : a low number of control points will result in a smoother curve. In this case, the position of the knots can be optimized like in [32]. In the other approach, a relatively large number of control point and a uniform knot vector are used and the smoothness is constrained by a penalty on the second derivatives [7, 11]. For reasons further detailed in the next paragraphs, the second approach was judged more suitable for our task. The vessels are modeled with penalized splines, as introduced by [11]. For penalized splines, the optimization of the control points is based on a cost function with two terms. The first term takes into account the closeness to the data point and the second term the smoothness of the approximation spline. The parameter  $\lambda$  controls the balance between both closeness and smoothness. The cost function is defined as

$$f(P_0, \dots, P_{n-1}) = \sum_{k=0}^m |D_k - s(t_k)|^2 + \lambda \sum_{j=2}^n (P_j - 2P_{j-1} + P_{j-2})^2, \quad (2)$$

where  $t$  is a time parametrization vector which associates each data point to a position on the spline.

#### 4.1.2 Approximation strategy

Centerline data provides both the spatial coordinate (x, y, z) and radius r, two variables of different scale that might show different noise levels. For this reason, they must be approximated separately. The choice of penalized splines allows us to dissociate  $\lambda$  values for the position and the radius in a two-step approximation algorithm.

With this approach, the spatial and radius coordinates can be modeled by a single spline.

For the approximation, we use a uniform knot vector and a parametrization obtained by the chord-length method. The number of control points is set so that the non-penalized approximation curve (i.e produced by solving equation 2 with  $\lambda = 0$ ) has a root mean square distance from the original data lower than a given value, which is set in this work to  $10^{-1}$  for spatial coordinates and  $10^{-3}$  for the radius.

We first solve the linear system arising from equation 2 for the spatial coordinates  $(x,y,z)$  of the centerline data points. The system can be written as

$$P_{(x,y,z)} = (N^T N + \lambda_s \Delta)^{-1} N^T D_{(x,y,z)}, \quad (3)$$

where  $N$  is the matrix of representation of the basis spline functions and  $\Delta$  is the matrix representation of the difference operator which appears in the second term of the cost function 2. The optimal value for  $\lambda_s$  is obtained by minimizing the Akaike criterion  $AIC_2$ . A comparison study with other selection criteria for  $\lambda$ , such as the Bayesian information criterion or cross validation, detailed in section 6, led to the choice of  $AIC$ . Then, the linear system is solved for the data  $(t, r)$  where  $t$  is the time parametrization of each data points and  $r$  their radius value :

$$P_{(t,r)} = (N^T N + \lambda_r \Delta)^{-1} N^T D_{(t,r)}. \quad (4)$$

The value of  $\lambda_r$  is also selected by minimizing AIC on the time/radius data. The spatial coordinates and radius of the optimized control points are then concatenated to form the 4-coordinates control points of the final spline. Figure 1 illustrates this two-part approximation scheme. The proposed approximation method is compared with other conventional approximation methods regarding the robustness to noise and low sampling of the data points in section 6.1.

## 4.2 Bifurcations

In this part, we focus on modeling the bifurcations from centerline data.

### 4.2.1 Zakaria's model

[42] proposed a parametric model for non-planar bifurcations. Their model was validated in regard with both the anatomy and numerical simulation of blood flow and showed a good agreement with real cerebral bifurcations. It requires only a few physiological parameters and is well suited for reconstruction of bifurcations from sparse data. In this model, bifurcations are created by merging two tubes which represents the daughter vessels. The tubes are defined by a shared inlet cross section  $C_0$ , separate apical cross sections  $AC_1$ ,  $AC_2$  and outlet sections  $C_1$  and  $C_2$ . The apical cross sections  $AC_{1,2}$  are located at the apex point  $AP$  of the bifurcation, where both tubes merges. The outlet sections  $C_{1,2}$  are cut one diameter away from the apex. In total, five cross sections and their normals are required to build the model. A cross section  $C$  is considered circular and is represented by the three spatial coordinates of its center  $P_c$ , a radius  $r_c$  and a normal  $\vec{n}_c$ . The centerline of each tube is defined by a centerline  $spl_{1,2}$ . The first segment of the centerline connects the inlet

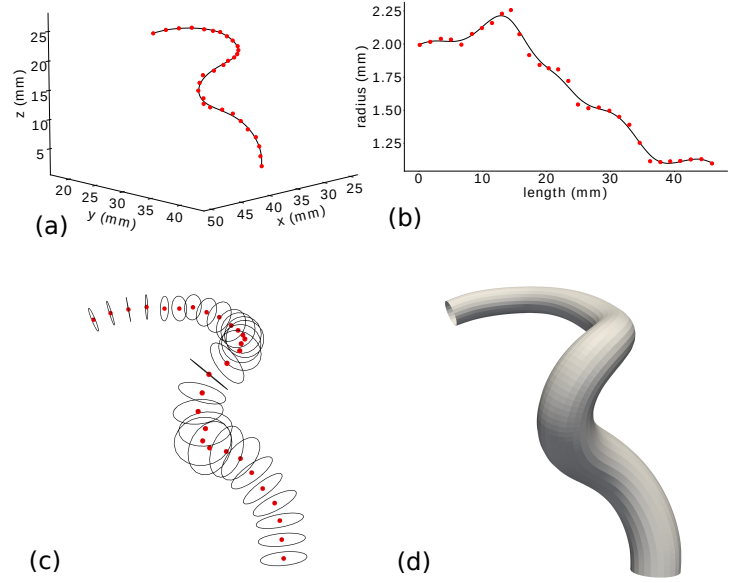


**FIGURE 1** Approximation of a noisy centerline with the proposed method. (a) and (b) show respectively the approximation of the spatial coordinates and the radius. Figure (c) shows the input centerline data in 3-dimensions as red dots with radius represented by black circles. In (d), the surface defined by the approximating spline-based model is represented.

section  $C_0$  to the apical section, the second connects the apical section to the outlet sections. The tangent of the centerline segments matches the normal of the joined cross sections. The radius along the segments evolves linearly between  $r_{C_0}$ ,  $r_{AC_{1,2}}$  and  $r_{AC_{1,2}}$ ,  $r_{C_{1,2}}$ . The bifurcation model is illustrated in Figure 2. The unphysiological sharp angle produced between tubes at the apex is rounded by a segment of constant radius of curvature  $R$ .

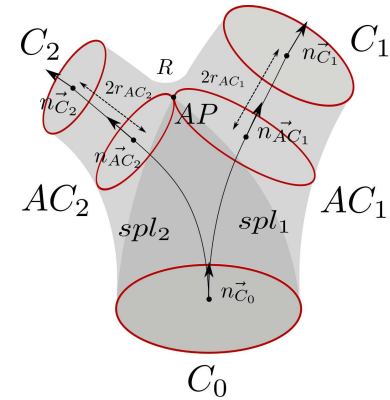


**FIGURE 2** Five cross sections bifurcation model introduced by [42].

### 4.2.2 Parameter estimation

We introduce an algorithm to estimate the parameters of the bifurcations directly from the input centerline data. The inlet data points (in light blue in Figure 3 (a)) are merged with each of the outlet data points (resp. in deep blue and green in Figure 3 (a)) to form two input centerlines going through the bifurcation, as shown in Figure

3 (b). The two vessels based on these centerlines are modeled independently by splines using the approximation strategy presented in section 4.1. The apex  $AP$  of the bifurcation is set as the point where the surface of the two vessel models first intersect (red dot on the Figure 3 (c)).  $AP$  is then projected on the model splines  $spl_1$  and  $spl_2$ . The tangent and position of the obtained projection points then define the normal and the center of the apical cross sections  $AC_1$  and  $AC_2$ . The outlet sections  $C_1$  (resp.  $C_2$ ) are computed in the same way from the evaluation of the spline where the length from the apex projection point is twice the radius of the apical section.

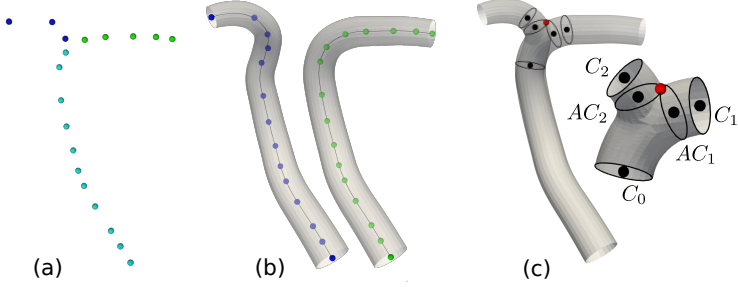


**FIGURE 3** Pipeline of the bifurcation parameter estimation. (a) shows the inlet and outlet data points, (b) the independent vessel models and (c) the parameter extraction and resulting bifurcation.

#### 4.2.3 Tangent continuity

The full vascular network model is created by assembling the vessels and bifurcations. In order to preserve the continuity of the different parts of the network, the end tangents of the extremities of the vessel models must match the normal of the inlet and outlet cross sections of the bifurcation models. For this, we introduce an additional constraint on the end point and tangent in the resolution of the approximation equations 3 and 4 used to model the vessels. A least square spline approximation with arbitrary end derivatives was proposed by [29]. We extend this approach to penalized splines and we propose a weaker constraint which fixes the end tangent while the derivative is free. We consider a spline  $s$  as defined by Equation 1, and because we work with clamped curves,  $s(0) = P_0$  and  $s(1) = P_{n-1}$ . Moreover,  $s'(0)$  (respectively  $s'(1)$ ) is in the same direction as vector  $P_1 - P_0$  (respectively  $P_{n-2} - P_{n-1}$ ). If we note  $S_0$  and  $S_{n-1}$  the fixed end points and  $T_0$  and  $T_{n-1}$  the fixed end tangents, the following new conditions are applied to the system 3:

$$\begin{cases} P_0 = S_0 \\ P_{n-1} = S_{n-1} \\ P_1 = P_0 + \alpha T_0 \\ P_{n-1} = P_{n-2} + \beta T_{n-1}, \end{cases} \quad (5)$$

where  $\alpha$  and  $\beta$ , the end tangent magnitude, are additional parameters to optimize. Those constraints guarantees the  $G_1$  continuity of the final network model.

## 5 Structured hexahedral meshing

### 5.1 Bifurcations

#### 5.1.1 Decomposition

For further meshing, a decomposition scheme is needed to split the bifurcation in three geometrical branches; one inlet branch and two outlet branches. The Figure 4 (b) gives an example of branch splitting using three separation planes. Antiga et al. [5] proposed a bifurcation decomposition scheme based on Voronoi diagram of the surface mesh. The decomposition they propose is robust to variations in input geometry and has been successfully used for hexahedral meshing [5]. However, it was not originally designed to obtain high quality meshes but to offer a robust mapping of bifurcations. Moreover, it requires a surface mesh to be computed and its transposition to centerline data is not straightforward. In this work, we introduced a decomposition scheme which relies on the spline and bifurcation models described above.

Three separation planes are defined by a set of five points; the apex point  $AP$ , which is already a parameter of the model, two center points  $CT_0$  and  $CT_1$  and two separation points  $SP_1$  and  $SP_2$ . As illustrated in Figure 4 (a), we first define the geometric center of the bifurcation  $X$ , as the barycenter of  $AP$ ,  $p_{m_1}$  and  $p_{m_2}$ , where  $p_{m_{1,2}}$  are the projection of the key points  $m_{1,2}$  located at the intersection of one centerline with the surface of the other vessel. The separation points  $SP_{1,2}$  are obtained by projecting  $X$  on the surface in the opposite direction from  $AP$ .

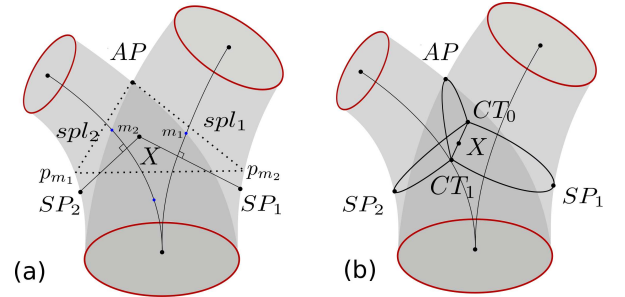


**FIGURE 4** Geometric decomposition of the bifurcation model. In (b), the end cross sections are represented in red and the separations planes in back.

Finally, the position of center points  $CT_0$  and  $CT_1$  is obtained by projecting  $X$  on the surface of the vessels. The direction of projection is the normal to the plane defined by the three points  $AP$ ,  $SP_1$  and  $SP_2$ . The separation points  $AP$ ,  $SP_1$  and  $SP_2$  are finally connected to the center points  $CT_0$ ,  $CT_1$  by arcs, which delineate a geometrical frontier between the branches of the bifurcation (see Figure 4 (b)), providing the desired branch decomposition. This decomposition enables to handle large radius difference between the daughter vessels. The barycenter  $X$  is naturally closer to the vessel with the smallest radius, which relaxes the angles between the separation planes and improves the quality of the resulting mesh.

#### 5.1.2 Surface meshing

In this step, we create the mesh grid connecting the end cross sections to the separation planes with a set of successive sections, as

illustrated in Figure 6. Each section of the mesh have a number  $N$  of nodes where  $N$  can be any multiple of 4. Figure 5 illustrates the process for constructing them. We first compute the  $N$  nodes of the end sections  $C_0$ ,  $C_1$  and  $C_2$ . A normalized reference vector  $ref_C$  which minimizes the rotation with the separation points  $SP_{1,2}$  is defined for each end cross section  $C$ . The nodes of the end sections are placed on the outline of the cross section, with evenly spaced angles starting by  $ref_C$  and rotated counterclockwise. The nodes of the separation planes are positioned with equally sampled angles along the arcs which join the separation point  $AP$ ,  $SP_1$  and  $SP_2$  to both center points  $CT_0$  and  $CT_1$ .

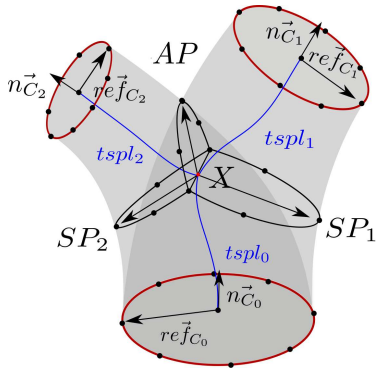


**FIGURE 5** Computation of the nodes (black dots) of the end cross sections and the separation planes for  $N = 8$  and splines  $tspl_{1,2,3}$ .

Once the nodes of the end section and the separation half-sections are computed, they are connected to form a surface mesh. The nodes of  $C_0$  are connected to the nodes of the half-sections defined by  $SP_1$  and  $SP_2$ , and the nodes of  $C_{1,2}$  are connected respectively to the nodes of the half-sections  $SP_{1,2}$  and  $AP$ .

We first define an initialization of the 3D trajectory that connects two nodes, as shown in the left column of Figure 6. This initialization is an approximation which is used to control the topology and geometry of the final mesh grid, but it does not necessary lies on the exact surface of the bifurcation at this point. The initial trajectories are evenly sampled with  $n$  nodes, where  $n$  determines the number of cross sections to compute along a given branch. This number is proportional to the radius of the end section of the branch, by a coefficient  $d$  which can be adjusted to obtain the intended density of faces in the mesh.

The nodes are then projected radially to the surface of the two vessels, as illustrated in the right column of Figure 6. The direction of the projection is important to maintain the quality of the faces of the initial grid after projection. Ideally, the nodes of the initial trajectory must be displaced only radially from the center of the branch vessel. However, the shape splines  $spl_1$  and  $spl_2$  does not constitute a good approximation of the centerline of the branches joining the geometric center of the bifurcation. For this reason, we create another set of splines  $tspl_{1,2,3}$  connecting the center of each end section to the center  $X$  of the bifurcation, represented in blue in Figure 5. The nodes are projected to the surface of the bifurcation model according to the normal of this new set of splines.

The properties of the resulting mesh depends on the initial trajectory approximation. Figure 6 illustrates the meshes obtained af-

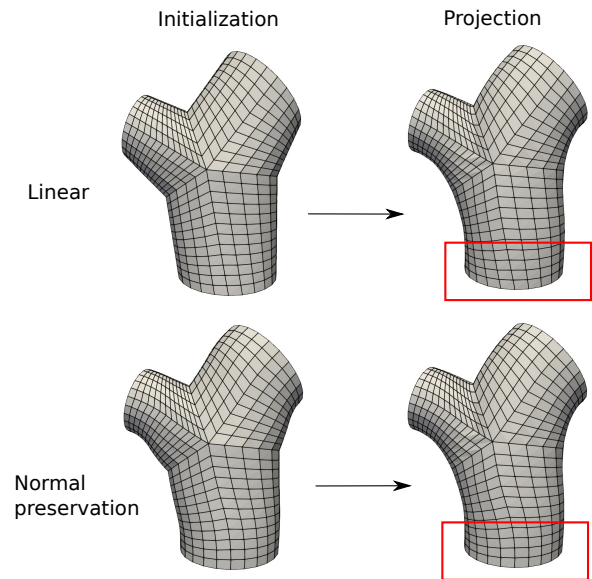


**FIGURE 6** Initial surface mesh and mesh after projection for the two types of initialization considered. The red squares emphasize the impact of the two types of initialization on the final mesh.

ter projection considering two types of initialization. The first row shows the simple case where the nodes of the end sections are linearly connected to the nodes of the separation geometry. In the second row, connection trajectories are computed so that the normal of the end sections is preserved in the output surface mesh. Both approximations allow to preserve the topology of the grid and the quality of the faces after projection. The initial trajectories with normal preservation are closer to the actual surface of the bifurcation, there is less displacement of the nodes during projection. Moreover, the preservation of the normal of the end sections enables to include the bifurcation mesh in larger arterial network; the connecting curves can be smoothly extended to downstream vessels. In the rest of this work, we use the normal preserving initialization.

### 5.1.3 Relaxation

The projection step of the meshing method results in an uneven sampling of the nodes along the trajectories and can lead to faces with heterogeneous size or important skewness. Moreover, a rupture of continuity is observed when the curves crosses the separation between two branches. Those unwanted features are corrected by relaxation of the nodes of the surface mesh. Mesh smoothing methods are an easy way to reduce the skewness of faces, however it triggers important deformations of the general shape of the model. To avoid deformations, [38] proposed to combine smoothing with a back projection on the surface. Following this approach, an iteration of Laplacian smooth (relaxation factor of 0.8) is first applied to the bifurcation mesh, then the nodes are projected back to the original surface. To prevent cross sections from intersecting, the projection is made in the direction of the line connecting the center of the cross section to the node to project. This process can be repeated until the relaxation is satisfying. Figure 7 displays a bifurcation mesh after 1 and 5 relaxation iterations. The faces are colored according to their geometric quality, measure by the scaled Jacobian. We

observe that while the shape of the model is preserved, the quality of the faces near the separation plan is improved, and the trajectories smoothly crosses the separation plans. Based on the average quality of the faces, we estimate that 5 relaxation iterations are sufficient.

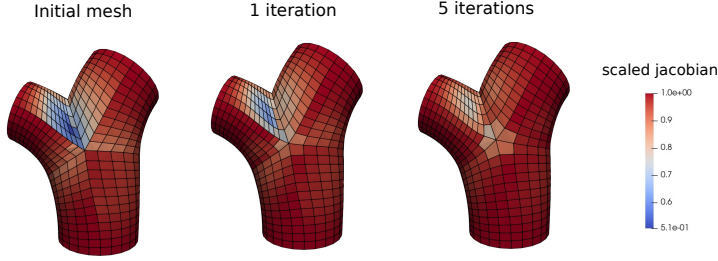


**FIGURE 7** Original bifurcation mesh and mesh after 1 and 5 relaxation iterations. The scaled Jacobian is used to measure the quality of the cells between  $-1$  (poor quality) and  $1$  (high quality).

#### 5.1.4 Apex smoothing

The last step of the bifurcation meshing is the smoothing of the apical region. The model presents an unwanted sharp angle where the two vessels merge. The curvature in the apex regions impacts the pressure and velocity fields obtained by numerical simulation, as shown by [15]. Conventional mesh smoothing methods (e.g Laplacian, Taubin smoothing) are fast and can produce smooth meshes with high quality faces. However as they are global methods, they struggle to generate important local deformations. [42] proposed to smooth the apex region by projecting the nodes on a sphere of given radius, rolling on the surface. This method is accurate, but it is computationally expensive and might not preserve the quality of the cells in the case of hexahedral meshes. Taking advantage of the topology of the proposed surface mesh, we reduced this complex 3-dimensional problem to a 2-dimensional problem.

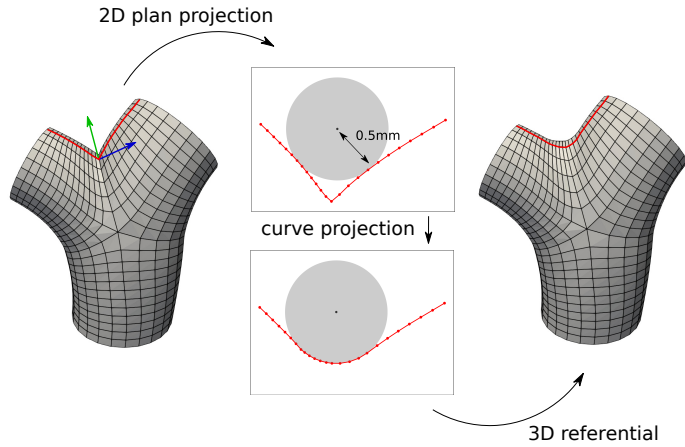


**FIGURE 8** Illustration of the apex smoothing pipeline.

Figure 8 illustrates the proposed smoothing method. The 3D polylines connecting two nodes of the end sections of the bifurcation are extracted (e.g, the curve in red on Figure 8). They are then projected on the 2D plane defined by the normal of the mesh at the separation

point and the normal of the separation plane (resp. green and blue arrows on Figure 8). A circle whose radius correspond to the desired apex radius of curvature is rolled along the 2D curves. The position of the circle where it is in contact with a further part of the curve is mathematically computed. The points located under the circle are moved to its outline, while preserving their original sampling. Finally, the new coordinates of the points are projected back on the original 3D referential to form the output surface mesh.

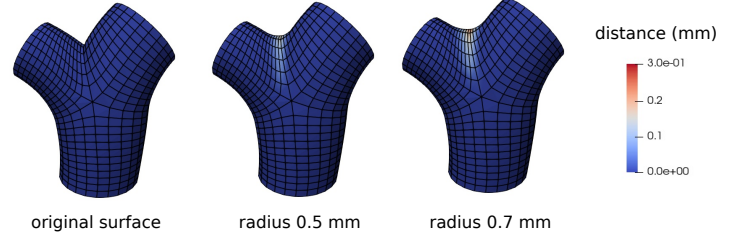


**FIGURE 9** Apex smoothing with different radius of curvature values. The colormap encodes the local distance to the original mesh, on the left.

The described smoothing method enables to control the direction of projection and the sampling of the projected nodes. Therefore, the quality of the faces is preserved. As shown in Figure 9, the smoothing is very local and does not affect the shape of the vessels outside of the apical region.

#### 5.1.5 Planar n-furcations

If the cerebral arterial network is composed of a majority of bifurcations, multifurcations may also be present (e.g trifurcations are frequently found on the basilar artery). To address this requirement, we generalized the model of [42] to planar n-furcations. The generalized n-furcation model is built with  $n - 1$  splines,  $2n + 1$  cross sections and  $n - 1$  apex points, as illustrated for the case  $n = 3$  in Figure 10 (a). We adapted the decomposition scheme presented in section 5.1 to compute  $n + 1$  separation plans, as in Figure 10 (b). Figure 10 (c) shows an example of planar trifurcation mesh obtained with this generalization.

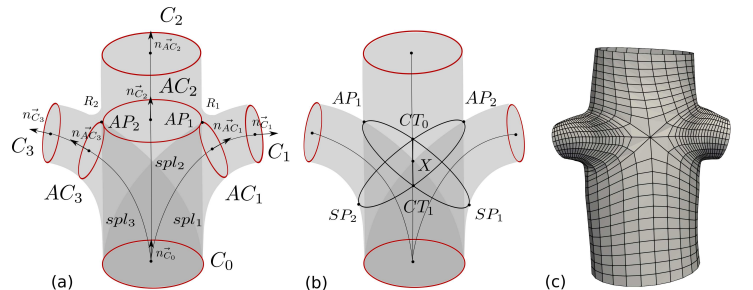


**FIGURE 10** (a) and (b) respectively illustrates the parametric model and the branch decomposition scheme for a trifurcation. (c) shows an example of trifurcation mesh.

## 5.2 Vessels

For the vessels, we adapted the meshing method proposed by [13] to the parametric model proposed in section 4.1 in order to obtain surface and volume meshes.

### 5.2.1 Surface meshing

To mesh the surface of a vessel, the spline model is evaluated at a set of time values equally sampled in the  $[0, 1]$  interval. Those values are used to set the center position and radius of the cross sections along the vessel (i.e the longitudinal resolution of the mesh). The density of cross sections (number of sections per  $mm$ ) is proportional to the mean radius of the vessel, with a proportional coefficient  $d$  which is set by the user. From each center positions,  $N$  nodes are radially projected on the model surface to form a circular cross section. The projection vector is swept along the centerline and avoids twisting between the sections. The successive sections are connected to each other to form the mesh faces. In the case of vessels connecting one bifurcation to another, an extra rotation is smoothly applied to the cross sections along the vessels so that the last vessel section is aligned with the first section of the next bifurcation.

### 5.2.2 Volume meshing

The volume of the vessel is meshed following the method of [13]. From each cross section of the surface mesh, a structured O-grid pattern is created. It has 3 different areas, including the boundary layers, intermediary layers and a central block. The relative size  $\alpha$ ,  $\beta$ ,  $\gamma$  of the areas, the number  $N_\alpha$  of boundary layers and the number  $N_\beta$  of intermediary layers can be adjusted. The separation planes of the n-furcations are handles by combining  $n + 1$  halves grids. The successive O-grid patterns are connected to form the hexahedral cells of the volume mesh, as showed in Figure 11.

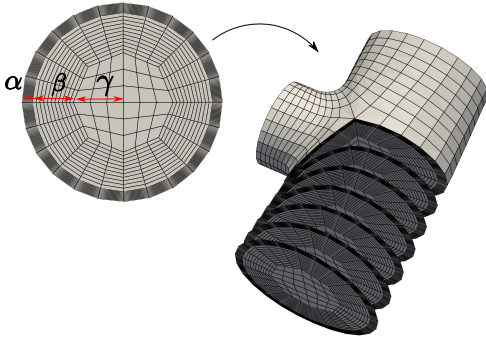


**FIGURE 11** Illustration of the O-grid pattern and volume meshing method.

## 6 Results

In this section, we evaluate both the modeling and the meshing methods proposed. The robustness and accuracy of the proposed vessel modeling method is assessed in an comparative study performed on a synthetic dataset of distorted centerlines. The performance of the

meshing method is measured in terms of cell quality and computational time.

## 6.1 Vessel model evaluation

In this part, we evaluate the robustness of the approximation method presented in section 5.2 to noise and low sampling of the data points.

### 6.1.1 Validation dataset

For this evaluation, we built a dataset of ground truth vessel models. Four surface meshes of cerebral arteries from the Aneurisk database were selected. For each mesh, a single vessel starting from the inlet of the network and ending at an outlet was selected so that it does not include pathologies but go through bifurcations, where we generally observe high curvature and big radius change. The selected vessel centerlines were extracted with a good resolution and low noise using the VMTK software. The obtained high quality centerline data points were then approximated by a 4-coordinate spline  $s$  that constitute the ground truth. The control points were manually added and the accuracy of the fitting of the spatial coordinates, radius and first derivatives were checked visually until the approximation was judged satisfying. Ground truth vessels and their creation process are illustrated in supplementary material, section 1.1.

To evaluate the robustness of our approach, those ground truth data were distorted to mimic defects commonly observed in realistic centerline data; low sampling and noise. Spatial noise and radius noise were applied separately, as they might differ in level. To generate spatial noise, the data points were displaced from their original position. The magnitude of displacement is randomly picked from a zero-centered Gaussian distribution with standard deviation  $\sigma_{spatial}$ . In order not to affect the radius values, the direction of the displacement is normal to the ground-truth spline  $s$ . Random radius noise is generated randomly from a zero-centered Gaussian distribution of standard deviation  $\sigma_{radius}$  and added to the ground truth radius. In both case, the applied standard deviation value is proportional to the point radius, as indicated in Table 1, in order to keep a similar levels of noise between big and small vessels. Finally, low sampling is obtained by removing data points along the centerline to reach target point densities.

**TABLE 1** Parameters used for the distortion of the ground-truth centerlines

density ( $mm^{-1}$ )	2	4	10	16	20
$\sigma_{radius}(mm)$	$0.01r$	$0.05r$	$0.1r$	$0.3r$	$0.5r$
$\sigma_{spatial}(mm)$	$0.01r$	$0.05r$	$0.1r$	$0.3r$	$0.5r$

For each density value in Table 1, ten combination of noise parameters are used, spatial and radius noise being added separately. Radius noise is applied to the ground-truth data with parameters  $\sigma_{radius}$  as given in Table 1 while the spatial noise is set to 0. Then spatial noise is applied with parameters  $\sigma_{spatial}$  as given in Table 1 while the radius noise is nul. Each noise combination is repeated three times to account for stochastic effect; we get 30 data per density value, thus 150 in total. This is done for the four vessels of the ground-truth dataset, bringing the number of data in the distorted dataset to 600.

### 6.1.2 Approximation methods

To demonstrate the robustness and the accuracy of the proposed approximation strategy presented in section 4.1, we compared it to approximation methods commonly used in the literature. If they claim to use splines or Bezier functions, few authors provided details on the approximation method employed. For this reason, we implemented four commonly used approximations methods with incremental complexity - including the original penalized splines proposed by [11] - in order to emphasize the contributions of the proposed method.

- **Global Non-Penalized (GNP)** : In this basic approach, the control points are optimized without smoothness penalty in the cost function (Equation 2 with  $\lambda = 0$ ). The number of control points is set to match the RMSE threshold given in section 4.1, paragraph 2. We call it global because spatial and radius dimensions are not addressed separately.
- **Global Non-Penalized with Akaike criterion (GNP-AIC)** : Optimizing the number of control points to obtain the desired spline smoothness is a common approximation method in the literature. In this approach, the optimal number of control points minimizes the Akaike information criterion ([1])  $AIC_1$  :

$$AIC_1 = m \times \log(SSE) + 8(n + p). \quad (6)$$

where  $m$  is the number of data points,  $p$  the degree of the spline,  $n$  the number of control points and SSE is the sum squared error from the data points, including their four coordinates.

- **Global Penalized with Akaike criterion (GP-AIC)** : This approach corresponds to the original approximation by penalized splines described in [11]. It uses the same global approach as in GNP, but with a smoothing penalty defined with a parameter  $\lambda \neq 0$  as in Equation 2.
- **Spatial coordinates and Radius Penalized with Akaike criterion (SRP-AIC)** : The approximation strategy that we propose in this work penalizes spatial and radius dimensions separately. The comparison of our strategy with GP-AIC allows to evaluate the contribution of treating the spatial and radius coordinates individually.

In methods GP-AIC and SRP-AIC, the criterion used to optimize the  $\lambda$  values is another formulation of the Akaike information criterion ( $AIC_2$ ), adapted to penalized splines, as proposed by [11]:

$$AIC_2 = m \times \log(SSE/m) + 2tr, \quad (7)$$

where  $tr$  is the trace of the matrix  $H = N(N^t N + \lambda \Delta)^{-1} N^t$ .

Unlike  $AIC_1$ , it is not employed to choose an optimal number of control points but to select the optimal value for the smoothing parametre  $\lambda$ . This criterion was compared to other criteria of the literature ; the corrected Akaike information criterion of [20], the Schwarz's Bayesian criterion of [35], the cross validation criterion and generalized cross validation criterion of [7]. According to this study, given in supplementary material (section 1.3), the Akaike criterion yielded the best results on our data.

### 6.1.3 Quality metrics

A total of six quality metrics were selected to evaluate the approximation strategies presented in the previous paragraph. To build an accurate measure of distance between the ground-truth spline  $s$  and the approximation spline  $\hat{s}$ , we project one curve on the other. As illustrated in Figure 12, two matched sets of time parameters are built. The spline  $s$  is equally sampled with a time vector  $t$ , then projected on  $\hat{s}$  according to the minimum distance to form the matched time vector  $T$ .

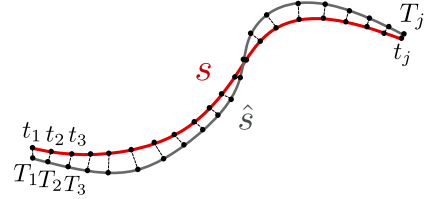


**FIGURE 12** Matching time parameters by minimum distance projection from  $s$  onto  $\hat{s}$

Once the projection is performed, the matched values can be compared. We use the root mean squared error (RMSE) as a measure of the closeness of the approximation spline to the ground-truth spline. The spatial coordinates and the radius values are treated separately in the evaluation. We note  $RMSE_{radius}$  (respectively  $RMSE_{spatial}$ ) the root mean squared error of the radius (respectively the spatial coordinates). In order to have a robust comparison between the curves, the projection is computed in both ways (from  $s$  to  $\hat{s}$  and from  $\hat{s}$  to  $s$ ) and the final RMSE value is the average of the RMSE yielded by both projections.

The accuracy of the first derivatives of the model is evaluated by the metrics  $RMSE_{der_{spatial}}$  and  $RMSE_{der_{radius}}$ . As curvature is commonly considered in hemodynamic studies, the model performance with regard to the centerline curvature is also measured, by the metric  $RMSE_{curv}$ . Finally, the length of the vessel affects the delay of blood arrival between inlet and outlet of the vascular tree in numerical simulations. Therefore, the difference  $L_{diff}$  of length between the ground-truth and the approximated centerline was considered.

### 6.1.4 Results

As the spatial and radius distortions are not comparable in nature and magnitude, the evaluation results are presented in two different tables. Table 2 (respectively Table 3) shows the mean values of the six quality criteria for the four methods after radius noise (respectively spatial noise) addition. As expected, the non-penalized model (GNP) is sensible to the added noise and performs poorly for all radius-related metrics. In Figure 13, the radius estimation error is clearly visible on the vessel produced by this method. In the same way, the spatial-related metrics are impacted when spatial noise is added (Table 3). In addition, a tendency to overfit the data is observed in Table 2, causing surprisingly high spatial error. The overfitting and noise problems are partially solved by optimizing the number of control points with method GNP-AIC. However, this approach still yields a poor approximation of the derivatives : as the number of control points is lower, the space between data points

might not be correctly interpolated, which particularly impacts the curvature values.

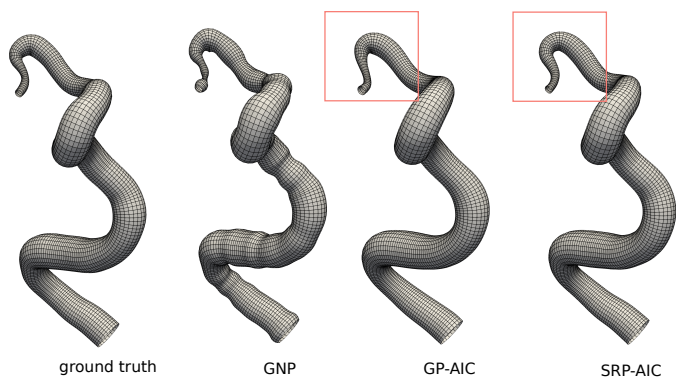


**FIGURE 13** Mesh resulting from the approximation of distorted data ( $density = 1mm^{-1}$ ,  $\sigma_{radius} = 0.1$ ) by three of the methods compared in section 6.1.

The penalized approximations GP-AIC and SRP-AIC enabled to drastically improve the estimation of the derivatives and curvature. Finally, the advantage of SRP-AIC over GP-AIC is demonstrated both in the result tables 2 and 3 and in Figure 13. The global smoothing penalty used in GP-AIC forces a trade-off between the radius and spatial accuracy. In Figure 13, the radius of the vessel produced by GP-AIC is very similar to the ground-truth vessel, but in return the trajectory of the centerline appears too smoothed. On the other hand, both the radius and trajectory of the vessel produced with SRP-AIC is closer to the ground-truth. As a conclusion of this comparison, the proposed approximation method shows a very good robustness to the defects of the input data while enabling to simultaneously and accurately model the vessel centerline and radius. More results are provided in supplementary material, section 1.2.

**TABLE 2** Overall evaluation of the approximation methods : mean values of the quality criteria for all the centerlines distorted by radius noise addition. The cells in gray corresponds to the lowest error for each metric.

	GNP	GNP-AIC	GP-AIC	SRP-AIC
RMSE <sub>spatial</sub>	8.462	0.034	0.053	0.029
RMSE <sub>radius</sub>	17.523	0.095	0.042	0.043
RMSE <sub>der<sub>spatial</sub></sub>	0.218	0.118	0.042	0.009
RMSE <sub>der<sub>radius</sub></sub>	0.391	0.214	0.032	0.032
RMSE <sub>curv</sub>	1919.428	190.531	0.060	0.035
L <sub>diff</sub>	718.906	0.057	0.207	0.004

## 6.2 Mesh quality

In CFD, the accuracy and stability of the simulation is affected by the quality of the mesh. In order to evaluate this quality, we computed the scaled Jacobian of the cells in the meshes generated with the proposed method. The scaled Jacobian ranges from -1 (worst quality) and 1 (best quality). Negative values indicate invalid cells. The volume meshes for 60 patients from the BraVa database were generated (see section 7.3 for details), with the following parameters ;  $N = 24$ ,  $d = 0.2$ ,  $\alpha = 0.2$ ,  $\beta = 0.3$ ,  $\gamma = 0.5$ ,  $N_\alpha = 10$ ,

**TABLE 3** Overall evaluation of the approximation methods : mean values of the quality criteria for all the centerlines distorted by spatial noise addition. The cells in gray corresponds to the lowest error for each metric.

	GNP	GNP-AIC	GP-AIC	SRP-AIC
RMSE <sub>spatial</sub>	0.511	0.152	0.099	0.096
RMSE <sub>radius</sub>	0.008	0.009	0.018	0.007
RMSE <sub>der<sub>spatial</sub></sub>	0.314	0.343	0.075	0.076
RMSE <sub>der<sub>radius</sub></sub>	0.015	0.019	0.021	0.013
RMSE <sub>curv</sub>	1.524	2.362	0.085	0.091
L <sub>diff</sub>	50.180	15.071	0.252	0.207

$N_\beta = 10$ . The cells of the bifurcations and vessels are evaluated separately. Failed bifurcations and vessels (see section 7.3) were excluded from the study. The histograms of scaled Jacobian for the 60 patients is given Figure 14, together with an example branch.

As shown in the image (a) of Figure 14, the bifurcations are the most challenging structures to mesh. The lower quality cells are mainly localized in the bifurcation separation planes. Nevertheless, we achieved a very good overall quality for bifurcation cells, with 71% of the cells with scaled Jacobian value higher than 0.9. The vessel cells have a even better quality, with 95.7% of the cells having a scaled Jacobian higher than 0.9. In terms of mesh quality, our method improves the state of the art. Indeed, only 49% of the cells have a scaled Jacobian above 0.9 in average on the distributions given for three large cerebral networks in [13]. This proportion goes up to 62% of the cells of the abdominal aortic artery geometry meshed by the method of [41]. Finally, in [9], between 65% and 82% - depending on the case and the cell density - of the cells of the aortic arch meshed have a scaled Jacobian value between 0.8 and 1. Quantitatively, our method gives better results, especially given that the histograms for the other methods were computed on all the cells, both bifurcations and vessels. However, we bear in mind that the study of [9] and [41] focuses on arterial geometries that differs from our study.

## 6.3 Computation time

The computational time of the modeling and meshing steps for five patients of the BraVa database were computed. The results for three of them are given in Table 4. The average time for modeling a large cerebral vascular network is about 16 minutes. The time for the volume meshing step is given in Table 4 for different cell densities. The average meshing time goes from 24.6 minutes for a the coarse mesh to 49.7 minutes for a fine mesh. We want to stress that this study was performed on large networks, with a high number of bifurcations (around 100) and vessels (around 200). The meshing time increases with the number of bifurcations and vessels, while the modeling time is affected by the number of data points.

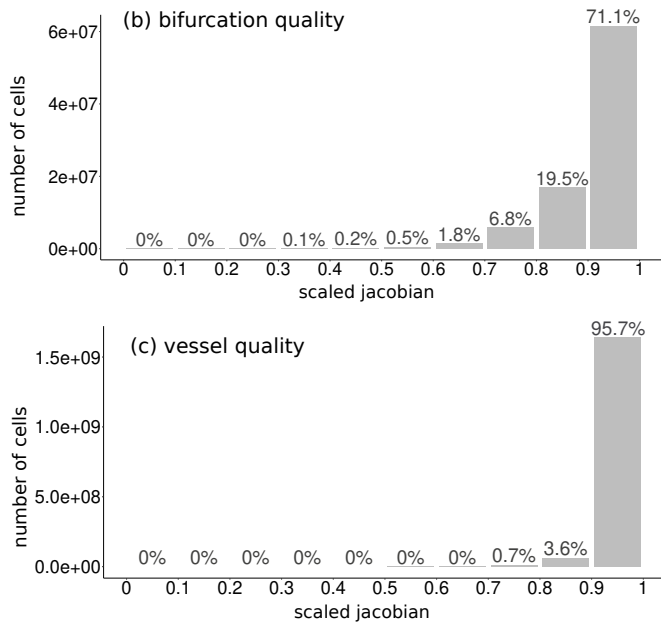
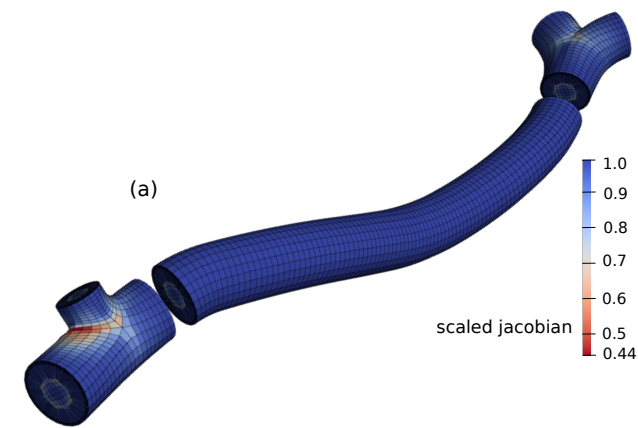


**FIGURE 14** Distribution of the scaled Jacobian values of the mesh cells. The histogram (b) represents the quality of bifurcations cells and the histogram (c) the quality of vessels cells. The image (a) illustrates the location of high and low quality cells within a mesh.

**TABLE 4** Computational time required to model and mesh large vascular networks from the BraVa dataset.

id	furcation (#)	vessel (#)	data point (#)	modeling time (min)	cells (#)	meshing time (min)
P1	96	194	2816	11.3	1389k	20.4
					1853k	25.7
					2316k	31.2
					2779k	38.4
P2	101	203	3531	18.3	1916k	27.5
					2555k	38.2
					3193k	49.1
					3832k	67.5
P3	107	216	3474	16.8	1737k	26.3
					2316k	36.1
					2895k	44.2
					3474k	55.9

Besides, a large part of the meshing time corresponds to the computation of the surface nodes ; in average 17.4 minutes for a coarse mesh and 34.8 minutes for a fine mesh. The volume mesh is generated directly from the nodes of the surface mesh without recomputing them. Finally, meshing can be run in parallel, by splitting the network into parts to be meshed on different CPUs. Using 12 CPUs, we were able to reduce the meshing computational times given in the Table 4 by a factor 5.

## 7 Applications

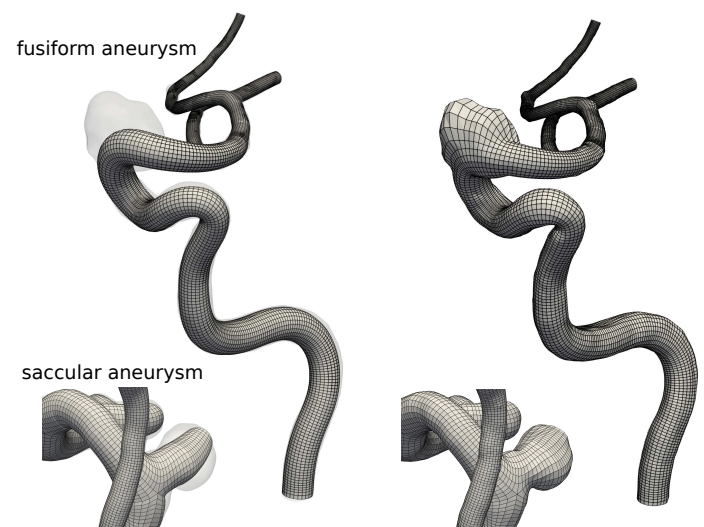
Several applications of our framework are proposed in this section.

### 7.1 Deformation

The proposed model is based on the assumption that vessel cross sections are circular, which is limiting when dealing with pathological vessels. A way to address this limitation is to deform the cross sections to match a target surface as a post processing. If the user input data is a surface mesh, we propose the following alternative use of our meshing framework:

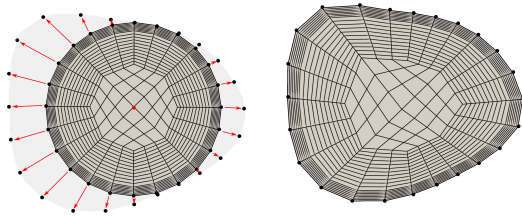
1. Extract the centerline from the surface mesh (using VMTK software for example),
2. Create a tubular mesh from the centerline using the proposed method,
3. Deform the tubular mesh to match the original surface.

Figure 15 illustrates an example of this pipeline to mesh arteries with aneurysms. In the deformation step, the nodes are individually projected onto the surface of the target mesh. To prevent the sections from intersecting, the nodes are projected radially from the section center.



**FIGURE 15** Structured hexahedral meshing of cerebral arteries with a fusiform or saccular aneurysm by deformation. On the left, the tubular mesh, obtained by our framework, is superimposed on the target surface. On the right, the mesh after projection.

As shown in Figure 15, saccular aneurysms are initially modeled as bifurcating vessels and then deformed. Because the shape of the volume mesh pattern depends on the position of the section nodes (cf Section 4.1), the deformation of the surface mesh is smoothly conveyed to the cells inside the mesh, as illustrated by Figure 16.



**FIGURE 16** Cross section pattern before and after deformation. The corresponding slice of the target surface mesh is represented in grey.

This pipeline is not limited to pathological vessels. It can be extended to remesh any vessel surface mesh with hexahedral cells.

## 7.2 Topology and geometry editing

The relationship between the vascular tree topology and geometry (e.g the different configuration of the circle of Willis, vessel angle) and the hemodynamics have been studied extensively in the literature, using ideal or patient specific models [6, 2]. In this context, the proposed meshing framework finds applications in creating and editing vascular models. Because only a few data points are required for the meshing, the bifurcation angles, the radius or trajectory of a vessel can be modified effortlessly. Figure 17 provides examples of such modifications. Topological and geometrical information are linked within our parametric vascular tree representation: this facilitates the identification and modification of the data points of a branch of interest. Moreover, the bifurcations are based on a parametric model whose parameters (cross sections, apex smoothing) can be adjusted. This model guarantees the physiological realism of the bifurcations even when artificial data points are used (e.g modeling vessels as straight lines). Thanks to the modeling of bifurcation as merging vessels, the removal of a bifurcation branch does not modify the trajectory of the other branch through the bifurcation part, as illustrated on the right of Figure 17. Branches and arterial territories inexpensively with a local re-computation of the model and mesh parts.

## 7.3 Large cerebral arterial network meshing

To demonstrate further the robustness and fully automatic nature of our method, we applied it to 60 patients of the BraVa dataset. The meshes produced for 8 of the patients are given in Figure 18. This dataset is considered as very challenging for several reasons. As the centerlines were extracted manually by medical doctors, they are noisy and have a low sampling. The superimposition of the centerline data points on the magnetic resonance angiography image in Figure 19 shows the high level of noise encountered in the input data, both in the radius estimation and the spatial positions. Besides, by computing the ratio of the number of data points on the total length of the connecting polyline, we estimated the average point density in the database to  $0.45 \text{ mm}^{-1}$ , which is very low.

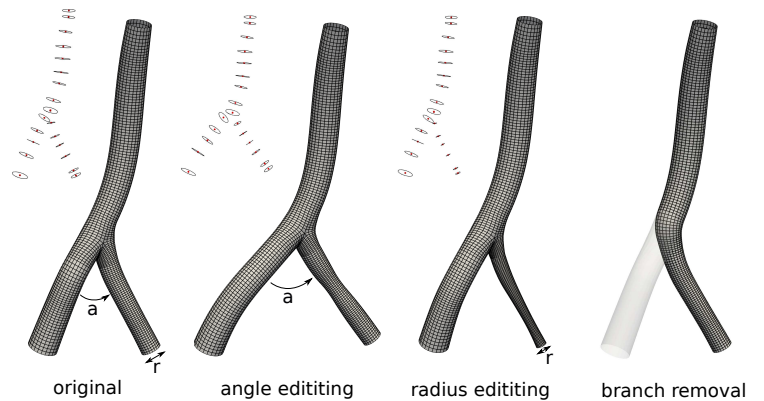


**FIGURE 17** Editing of a model of basilar artery using our framework. The bifurcation angle and the radius of the original vertebral artery are modified, one of the inlet vertebral arteries is removed. The centerline points and radius used to produce the meshes are represented on the top left for each case in which they were modified.

We evaluate the percentage of successfully meshed vessels and bifurcations separately, as the meshing method is different. The vessels or bifurcations with at least one cell with negative scaled Jacobian score are considered failed. With this strict definition, a total of 83% of the bifurcations and 92% of the vessels were successfully meshed.

The main reason for the failure of the vessel mesh is a too high curvature - mainly in the arteries with high tortuosity such as the internal carotid arteries - caused by a sharp angle in the input centerline. The main causes of failure for the bifurcations were very low bifurcation angles and misplacement of bifurcation points in the input data. This last case is illustrated on the image (b) of Figure 19. We can see that the bifurcation point in the centerline data was positioned too far downstream in the main vessel, causing one of the daughter vessel to go backwards from the direction of the flow with a sharp angle. As we use an oriented bifurcation model, it failed to correctly represent the geometry. The image (a) of Figure 19, on the other hand, illustrates a successful reconstruction of the trajectory of the vessel. Although the input centerline was very imprecise both in the radius estimation and point positions, we were able to produce a smooth model, closest to the vessel geometry as given by the medical image. Moreover, as shown in the insert of Figure 19 (a), even challenging topologies (e.g short connecting segment between bifurcations) can be successfully meshed with hexahedral elements. An image of all the meshes of the database, with failure areas highlighted is given in supplementary materials, section 1.3.

## 8 Conclusion

In this article, we addressed the problem of the reconstruction and meshing of large vascular networks from noisy, sparse centerlines. The proposed method is robust, accurate and automatic. It opens the way to CFD simulations in large vascular networks manually or semi-automatically extracted by medical doctors, with a minimal manual intervention. An original approximation method unifying the spatial and radius information in a single function is proposed to

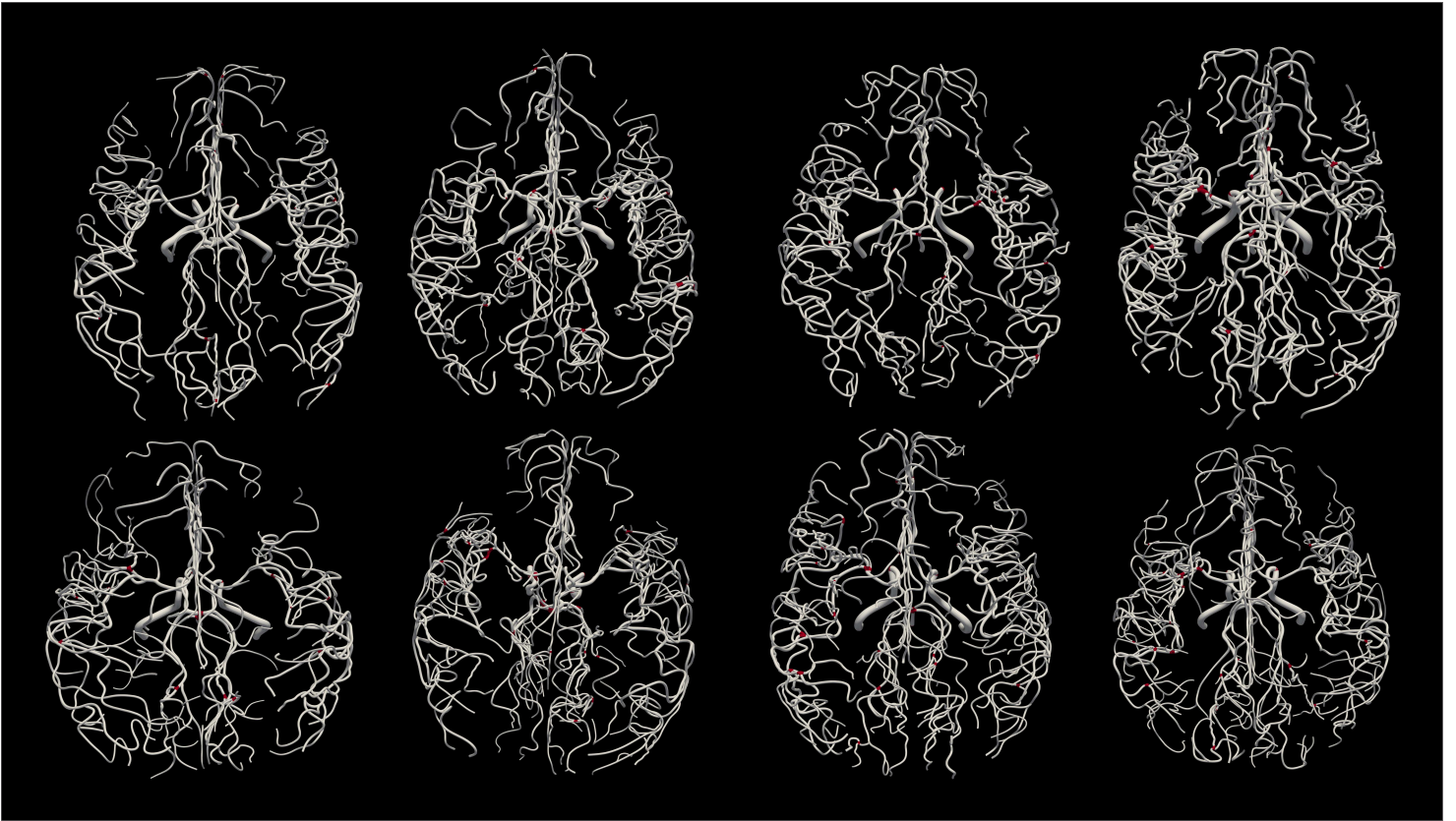


**FIGURE 18** Top view of 8 meshes among the 60 generated from the patients of the BraVa database. The bifurcations where the meshing algorithm has failed (i.e. at least one of the cells has a negative Jacobian) are represented in red. The cross sections of the vessels with cells of negative Jacobian values are also represented in red.

model the vessels. The use of a bifurcation model based on physiological parameters is associated with a new hexahedral meshing and smoothing techniques to produce bifurcations with a realistic shape and high quality cells in a reasonable time. Our method finds application in automatic meshing of large databases of vascular centerlines and hexahedral remeshing of non-tubular or pathologic vessels. It is well suited for the creation of realistic ideal vascular network models and the study of the impact of topological (branch removal) and geometrical (branch angle) on blood flow.

We acknowledge some limitations to this work. The pipeline was mainly tested on cerebral vascular networks so far, and non-planar bifurcations ( $n > 3$ ) that are common in other vessels (e.g. aorta) were not addressed. In addition, the robustness of the modeling and meshing method could be further improved as it failed on some cases. For this, we would like to integrate more physiological constraints on the bifurcation and vessel models such as a maximum curvature or maximum vessel angle for instance. Besides, we want to emphasize that our objective with this work is not to improve the performance of the segmentation or centerline extraction algorithms but to acknowledge the limitations of the realistic data and generate meshes as close as possible to the real anatomy from flawed centerlines and existing databases. Hence, the accuracy of the reconstruction depends on the accuracy of the input centerlines and might not be in total accordance with the real patient anatomy as has been shown in medical images. In order to address the issue of the agreement between the medical image and the centerline points position, we plan to develop a vas-

cular network editing software, with a relevant user interface. This interface will integrate the different methods (modeling, meshing, deformation, branch removal) described in the article and could also integrate editing functionalities enabling to modify the input centerline data points in accordance with the medical image in a 3D viewer. It would open vascular modeling and hexahedral meshing to medical doctors and non-expert users.

## Acknowledgments

We would like to thank Simon Tupin, who initiated this work and Erwan Maury for his contribution to the development of the apex smoothing method. Funding is acknowledged through AURA region (SIMAVC project) and ANR 20-CE45-0011 (PreSpin project).

## References

- [1] Hirotugu Akaike. Information theory and an extension of the maximum likelihood principle. *Proceedings of the Second International Symposium on Information Theory*, pages 267–281, 1973.
- [2] Martin Sandve Alnæs, Jørgen Isaksen, Kent-André Mardal, Bertil Romner, Michael K Morgan, and Tor Ingebrigtsen.

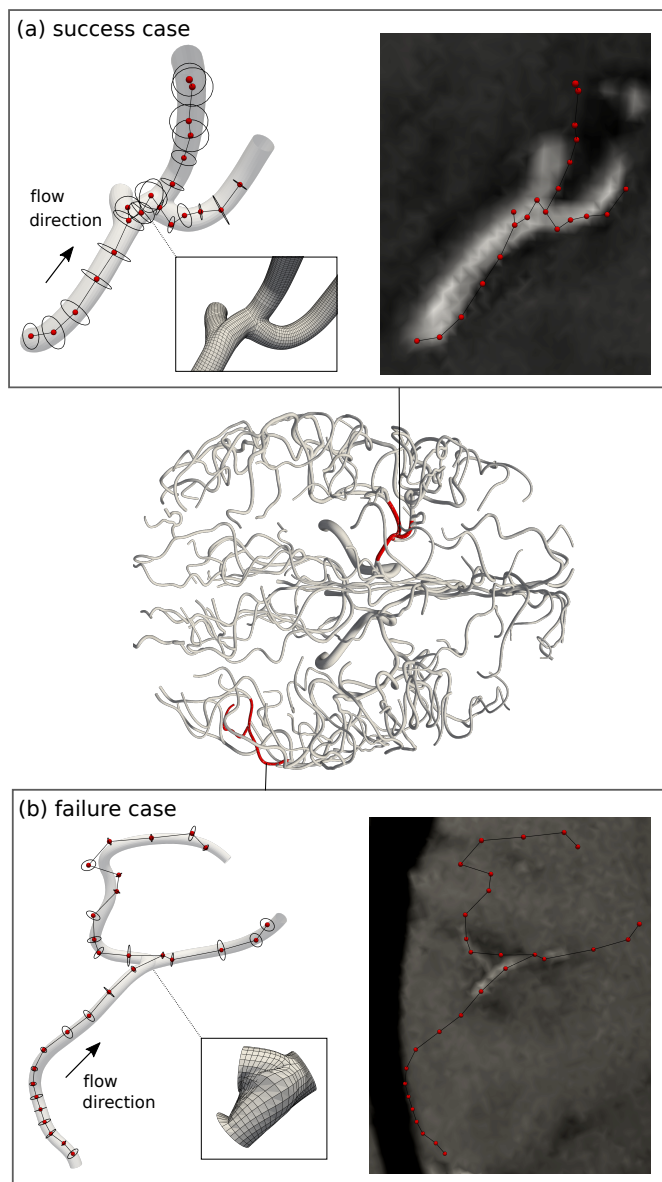


**FIGURE 19** Example of success and failure of our method for one patient of the BraVa database. The whole brain mesh is represented in the middle with focus on two parts of the network. For each focus, the original centerline data points are represented by red dots (center) and black circles (radius). The mesh obtained is superimposed on the data points, with an highlight on the relevant parts. On the right image the original centerline data points are overlaid on the original MRA image.

Computation of hemodynamics in the circle of willis. *Stroke*, 38(9):2500–2505, 2007.

- [3] Aneurisk-Team. AneuriskWeb project website, <http://ecm2.mathcs.emory.edu/aneuriskweb>. Web Site, 2012.
- [4] Luca Antiga, Bogdan Ene-Iordache, Lionello Caverni, Gian Paolo Cornalba, and Andrea Remuzzi. Geometric reconstruction for computational mesh generation of arterial bifur-

cations from ct angiography. *Computerized Medical Imaging and Graphics*, 26(4):227–235, 2002.

- [5] Luca Antiga and David A Steinman. Robust and objective decomposition and mapping of bifurcating vessels. *IEEE transactions on medical imaging*, 23(6):704–713, 2004.
- [6] BMW Cornelissen, JJ Schneiders, ME Sprengers, René van den Berg, P Van Ooij, AJ Nederveen, E Van Bavel, WP Vandertop, CH Slump, HA Marquering, et al. Aneurysmal parent artery-specific inflow conditions for complete and incomplete circle of willis configurations. *American journal of neuroradiology*, 39(5):910–915, 2018.
- [7] Peter Craven and Grace Wahba. Smoothing noisy data with spline functions. *Numerische mathematik*, 31(4):377–403, 1978.
- [8] Gianluca De Santis, Matthieu De Beule, Patrick Segers, Pascal Verdonck, and Benedict Verhegghe. Patient-specific computational haemodynamics: generation of structured and conformal hexahedral meshes from triangulated surfaces of vascular bifurcations. *Computer methods in biomechanics and biomedical engineering*, 14(9):797–802, 2011.
- [9] Gianluca De Santis, Matthieu De Beule, Koen Van Canneyt, Patrick Segers, Pascal Verdonck, and Benedict Verhegghe. Full-hexahedral structured meshing for image-based computational vascular modeling. *Medical engineering & physics*, 33(10):1318–1325, 2011.
- [10] Gianluca De Santis, Peter Mortier, Matthieu De Beule, Patrick Segers, Pascal Verdonck, and Benedict Verhegghe. Patient-specific computational fluid dynamics: structured mesh generation from coronary angiography. *Medical & biological engineering & computing*, 48(4):371–380, 2010.
- [11] Paul HC Eilers and Brian D Marx. Flexible smoothing with b-splines and penalties. *Statistical science*, 11(2):89–121, 1996.
- [12] Mahsa Ghaffari, Chih-Yang Hsu, and Andreas A Linninger. Automatic reconstruction and generation of structured hexahedral mesh for non-planar bifurcations in vascular networks. In *Computer Aided Chemical Engineering*, volume 37, pages 635–640. Elsevier, 2015.
- [13] Mahsa Ghaffari, Kevin Tangen, Ali Alaraj, Xinjian Du, Fady T Charbel, and Andreas A Linninger. Large-scale subject-specific cerebral arterial tree modeling using automated parametric mesh generation for blood flow simulation. *Computers in biology and medicine*, 91:353–365, 2017.
- [14] Jixiang Guo, Shun Li, Yim Pan Chui, Jing Qin, and Pheng Ann Heng. Mesh quality oriented 3d geometric vascular modeling based on parallel transport frame. *Computers in biology and medicine*, 43(7):879–888, 2013.
- [15] IV Haljasmaa, AM Robertson, and GP Galdi. On the effect of apex geometry on wall shear stress and pressure in two-dimensional models of arterial bifurcations. *Mathematical Models and Methods in Applied Sciences*, 11(03):499–520, 2001.

- [16] Xiaoxiao Han, Richard Bibb, and Russell Harris. Design of bifurcation junctions in artificial vascular vessels additively manufactured for skin tissue engineering. *Journal of Visual Languages & Computing*, 28:238–249, 2015.
- [17] Jiafa He, Chengwei Pan, Can Yang, Ming Zhang, Yang Wang, Xiaowei Zhou, and Yizhou Yu. Learning hybrid representations for automatic 3d vessel centerline extraction. In *International Conference on Medical Image Computing and Computer-Assisted Intervention*, pages 24–34. Springer, 2020.
- [18] Qingqi Hong, Qingde Li, Beizhan Wang, Kunhong Liu, Fan Lin, Juncong Lin, Xuan Cheng, Zhihong Zhang, and Ming Zeng. Accurate geometry modeling of vasculatures using implicit fitting with 2d radial basis functions. *Computer Aided Geometric Design*, 62:206–216, 2018.
- [19] Qingqi Hong, Qingde Li, Beizhan Wang, Jie Tian, Fei Xu, Kunhong Liu, and Xuan Cheng. High-quality vascular modeling and modification with implicit extrusion surfaces for blood flow computations. *Computer Methods and Programs in Biomedicine*, 196:105598, 2020.
- [20] Clifford M Hurvich, Jeffrey S Simonoff, and Chih-Ling Tsai. Smoothing parameter selection in nonparametric regression using an improved akaike information criterion. *Journal of the Royal Statistical Society: Series B (Statistical Methodology)*, 60(2):271–293, 1998.
- [21] Richard Izzo, David Steinman, Simone Manini, and Luca Antiga. The vascular modeling toolkit: a python library for the analysis of tubular structures in medical images. *Journal of Open Source Software*, 3(25):745, 2018.
- [22] Tim Jerman, Franjo Pernuš, Boštjan Likar, and Žiga Špiclin. Beyond frangi: an improved multiscale vesselness filter. In *Medical Imaging 2015: Image Processing*, volume 9413, page 94132A. International Society for Optics and Photonics, 2015.
- [23] Erwan Kerrien, Ahmed Yureidini, Jeremie Dequidt, Christian Duriez, René Anxionnat, and Stéphane Cotin. Blood vessel modeling for interactive simulation of interventional neuro-radiology procedures. *Medical image analysis*, 35:685–698, 2017.
- [24] Marek Kociński, Andrzej Materka, Andreas Deistung, and Jürgen R Reichenbach. Centerline-based surface modeling of blood-vessel trees in cerebral 3d mra. In *2016 Signal Processing: Algorithms, Architectures, Arrangements, and Applications (SPA)*, pages 85–90. IEEE, 2016.
- [25] David Lesage, Elsa D Angelini, Isabelle Bloch, and Gareth Funka-Lea. A review of 3d vessel lumen segmentation techniques: Models, features and extraction schemes. *Medical image analysis*, 13(6):819–845, 2009.
- [26] Mark H Longair, Dean A Baker, and J Douglas Armstrong. Simple neurite tracer: open source software for reconstruction, visualization and analysis of neuronal processes. *Bioinformatics*, 27(17):2453–2454, 2011.
- [27] Odysée Merveille, Hugues Talbot, Laurent Najman, and Nicolas Passat. Curvilinear structure analysis by ranking the orientation responses of path operators. *IEEE transactions on pattern analysis and machine intelligence*, 40(2):304–317, 2017.
- [28] Les Piegl and Wayne Tiller. *The NURBS book*. Springer Science & Business Media, 1996.
- [29] Les A Piegl and Wayne Tiller. Least-squares b-spline curve approximation with arbitrary end derivatives. *Engineering with Computers*, 16(2):109–116, 2000.
- [30] Maria José Melo Ramos-Lima, Ismênia de Carvalho Brasileiro, Tamires Layane de Lima, and Pedro Braga-Neto. Quality of life after stroke: impact of clinical and sociodemographic factors. *Clinics*, 73, 2018.
- [31] Laura M Sangalli, Piercesare Secchi, Simone Vantini, and Alessandro Veneziani. A case study in exploratory functional data analysis: geometrical features of the internal carotid artery. *Journal of the American Statistical Association*, 104(485):37–48, 2009.
- [32] Laura M Sangalli, Piercesare Secchi, Simone Vantini, and Alessandro Veneziani. Efficient estimation of three-dimensional curves and their derivatives by free-knot regression splines, applied to the analysis of inner carotid artery centerlines. *Journal of the Royal Statistical Society: Series C (Applied Statistics)*, 58(3):285–306, 2009.
- [33] Khalid M Saqr, Sherif Rashad, Simon Tupin, Kuniyasu Niizuma, Tamer Hassan, Teiji Tominaga, and Makoto Ohta. What does computational fluid dynamics tell us about intracranial aneurysms? a meta-analysis and critical review. *Journal of Cerebral Blood Flow & Metabolism*, 40(5):1021–1039, 2020.
- [34] Michiel Schaap, Coert T Metz, Theo van Walsum, Alina G van der Giessen, Annick C Weustink, Nico R Mollet, Christian Bauer, Hrvoje Bogunović, Carlos Castro, Xiang Deng, et al. Standardized evaluation methodology and reference database for evaluating coronary artery centerline extraction algorithms. *Medical image analysis*, 13(5):701–714, 2009.
- [35] Gideon Schwarz. Estimating the dimension of a model. *The annals of statistics*, pages 461–464, 1978.
- [36] Shin-ichiro Sugiyama, Kuniyasu Niizuma, Kenichi Sato, Sherif Rashad, Misaki Kohama, Hidenori Endo, Toshiki Endo, Yasushi Matsumoto, Makoto Ohta, and Teiji Tominaga. Blood flow into basilar tip aneurysms: a predictor for recanalization after coil embolization. *Stroke*, 47(10):2541–2547, 2016.
- [37] Chaman Singh Verma, Paul F Fischer, Seung E Lee, and Francis Loth. An all-hex meshing strategy for bifurcation geometries in vascular flow simulation. In *Proceedings of the 14th international meshing roundtable*, pages 363–375. Springer, 2005.
- [38] Vincent Vidal, Guillaume Lavoué, and Florent Dupont. Low budget and high fidelity relaxed 567-remeshing. *Computers & Graphics*, 47:16–23, 2015.

- [39] Samir Vinchurkar and P Worth Longest. Evaluation of hexahedral, prismatic and hybrid mesh styles for simulating respiratory aerosol dynamics. *Computers & Fluids*, 37(3):317–331, 2008.
- [40] Susan N Wright, Peter Kochunov, Fernando Mut, Maurizio Bergamino, Kerry M Brown, John C Mazziotta, Arthur W Toga, Juan R Cebal, and Giorgio A Ascoli. Digital reconstruction and morphometric analysis of human brain arterial vasculature from magnetic resonance angiography. *Neuroimage*, 82:170–181, 2013.
- [41] Guanglei Xiong, Suraj Musuvathy, and Tong Fang. Automated structured all-quadrilateral and hexahedral meshing of tubular surfaces. In *Proceedings of the 21st international meshing roundtable*, pages 103–120. Springer, 2013.
- [42] Hasballah Zakaria, Anne M Robertson, and Charles W Kerber. A parametric model for studies of flow in arterial bifurcations. *Annals of biomedical Engineering*, 36:1515, 2008.
- [43] Yongjie Zhang, Yuri Bazilevs, Samrat Goswami, Chandrajit L Bajaj, and Thomas JR Hughes. Patient-specific vascular nurbs modeling for isogeometric analysis of blood flow. *Computer methods in applied mechanics and engineering*, 196(29-30):2943–2959, 2007.